ADVANCED ENERGY MATERIALS
www.advenergymat.de

Light-Induced Ammonia Generation over Defective Carbon Nitride Modified with Pyrite

*Judith Zander, Jana Timm, Morten Weiss, and Roland Marschall**

Photocatalytic nitrogen fixation under ambient conditions is currently widely explored in an attempt to develop a sustainable alternative for the Haber–Bosch process. In this work, defect-rich carbon nitride, one of the most investigated photocatalysts reported in literature for ammonia generation, is combined with earth-abundant and bioinspired FeS_2 to improve the activity for ammonia production. By this combination, an activity enhancement of ≈400% compared to unmodified carbon nitride is achieved. The optimal FeS_2 loading is established to be 1 wt%, with ammonia yields of up to 800 µg L^{-1} after irradiation for 7 h. By detailed material characterization of the electronic and material properties of the composites before and after the photocatalytic reaction, it is revealed that NH_3 generation occurs not photocatalytically from N_2, but via a light-induced reduction of =N–CN groups adjacent to nitrogen vacancies in the structure of defect-rich carbon nitride. FeS_2 acts similar to a cocatalyst, enhancing the ammonia yield by π-back-donation from Fe-centers to the imine nitrogen of the defect-rich carbon nitride, thereby activating the structure and boosting the ammonia generation from cyano groups.

1. Introduction

The Haber–Bosch process is a large-scale industrial process for the production of ammonia (NH_3) from hydrogen (H_2) and nitrogen (N_2) gas at elevated pressures and temperatures. It is a well-established and optimized process, that is crucial for the production of fertilizers. Nevertheless, it still suffers from sustainability issues due to high energy requirements and the utilization of natural gas for the supply of H_2 in large, centralized power plants.[1] The photocatalytic nitrogen reduction reaction (NRR), that directly converts N_2 into NH_3 under (sun)-light irradiation at ambient conditions, presents a feasible alternative.[2,3] However, the NRR is a thermodynamically and kinetically unfavorable process due to the stable and inert nature of the N_2 molecule. Furthermore, the similar potentials for N_2 reduction and H_2 evolution impede a high selectivity in aqueous media so far. This imposes strident demands on an efficient and selective photocatalyst, that are not even close to be met even by the state-of-the art materials, thus highlighting the importance of continued research on the topic.[2,4,5] The low NH_3 yields further pose additional difficulties when it comes to accurate quantification, necessitating careful experiment control to avoid impurities and erroneous results. Discrepancies in the experimental conditions and a lack of standardized procedures further limit the comparability and reproducibility of photocatalytic NRR.[6–9]

Carbon nitride (CN) like polyheptazine imide, C_3N_4, are low cost, nontoxic polymeric materials with good light absorption characteristics, due to a band gap of ≈2.7 eV, which have received a lot of attention as an n-type photocatalyst during the past decade.[10,11] CN is commonly synthesized by thermal polymerization of organic precursor molecules, such as urea, melamine or cyanamide. The polymerization conditions, as well as the choice of the precursors have a strong effect on its structure and properties, by influencing the defect concentration, degree of polymerization, optical band gap, and surface area.[12] As-synthesized CN suffers from high recombination rates of photogenerated charge carriers. Therefore, alteration of the structure by doping or defect engineering and the formation of heterojunctions have been widely explored to improve the photocatalytic performance of CN.[13–24]

Some of the highest NH_3 yields in photocatalytic NRR have been reported using defective CN.[25–29] Owing to the polymeric structure of CN, the number of possible defects is vast and versatile.[18,20,21,30,31] A frequently exploited strategy for activity enhancement in CN is the introduction of nitrogen vacancies, which are of the same size as the nitrogen atoms in molecular N_2, and can thus act as efficient adsorption and activation centers.[30]

Another important class of defects are cyano or cyanamide groups, that act as electron-withdrawing groups, assisting in charge separation and suppressing recombination.[14,27,32] The NRR is supposed to proceed via a Mars–van-Krevelen mechanism for both defect types, making a distinction between the influence of cyano groups and nitrogen vacancies difficult. Intercalation of potassium was reported to assist in the replenishment of nitrogen in the structure, more specifically of the cyano groups, resulting in an NH_3 production rate of 3.42 mmol g^{-1} h^{-1}.[28] Treatment

J. Zander, J. Timm, M. Weiss, R. Marschall
Department of Chemistry
University of Bayreuth
95440 Bayreuth, Germany
E-mail: roland.marschall@uni-bayreuth.de

The ORCID identification number(s) for the author(s) of this article can be found under https://doi.org/10.1002/aenm.202202403.

DOI: 10.1002/aenm.202202403

of bulk CN with KOH, or direct incorporation of KOH into the synthesis recently emerged as a promising strategy for both the introduction of vacancies and of cyano groups. Zhou et al. treated bulk CN with KOH in ethanol, followed by solvent evaporation and annealing. They observed an abundance of cyano groups that assisted in charge separation and N_2 adsorption.[27] KOH has also directly been involved in the thermal polymerization of urea, likewise promoting the formation of cyano groups.[14] A similar result was obtained by Wang et al., using KOH in the thermal polymerization of dicyandiamide.[28] Etching with KOH was reported to mostly lead to the formation of vacancies. Still high NH_3 yields of 3.632 mmol g^{-1} h^{-1} were reported, together with a quantum efficiency of over 20%.[25]

Apart from defect engineering, research on semiconductor materials for artificial photosynthesis is still in its infancy compared to the process optimization in nature. The reduction of molecular N_2 has been realized under ambient conditions at the active centers of selected enzymes, termed nitrogenases. Three different classes of nitrogenases are distinguished, based on the composition of the active centers: all contain sulfur and iron atoms, but differ in the nature of additional constituents, one containing vanadium, one molybdenum and one solely iron.[33] This composition led to the exploration of several iron or molybdenum based compounds for the NRR.[34–42] One of the simplest iron and sulfur containing compounds is FeS_2, which is a nontoxic, stable, and earth-abundant mineral. It shows very high optical absorption and high charge carrier mobility, but its use in photoelectrochemical applications suffers from charge trapping and recombination.[43] Still, FeS_2 has been explored for photocatalytic dye degradation.[44–46] By itself it is reported to be inactive in photocatalytic NRR, due to unsuitable band positions, but it might still offer beneficial contribution in combination with other materials.[47,48] Thus, composites with FeS_2 have been employed for photocatalytic dye degradation, H_2 evolution, CO_2 reduction, and NRR.[49–54] Apart from improving the light absorption properties in composites, FeS_2 can act as an efficient electrocatalyst, which has been shown separately for the H_2 evolution, as well as for the NRR.[55–59] There have been also recent reports on the formation of heterojunctions of FeS_2 with CN and their photocatalytic application in organic dye and antibiotics removal.[60,61] The reported mechanism and band positions on which the proposed electron transfers are based, are notably different between the reports, requiring further investigation of the interaction between both materials.

In a bioinspired approach, we herein report the combination of the two earth-abundant semiconducting materials FeS_2 and defective CN for light-induced NH_3 generation. Exploiting the good light absorption and N_2 activation characteristics of the Fe–S system together with the reported high activity of defective CN, NH_3 yields of up to 800 µg L^{-1} can be achieved in the course of the reaction (7 h), which equals to an activity enhancement by around 400% compared to bulk CN. By detailed characterization of the electronic and material properties of the composites before and after reaction, we show that FeS_2 decoration weakens the bonds of CN-terminating imine groups in the vicinity of nitrogen defects by back donation. This facilitates the reduction of terminal cyano groups under light irradiation toward NH_3, with H_2 being the only by-product.

2. Results and Discussion

2.1. Material Synthesis and Characterization

The X-ray diffraction (XRD) patterns of the KOH-treated CN (V_N-CN) show the typical two broad reflections at 13° 2θ and at 27.4° 2θ, corresponding to in-plane order and interplanar stacking, respectively, with a d-spacing of ≈ 0.326 nm (Figure S2, Supporting Information).[62] The structure of CN obtained via thermal polymerization is best described by a model of parallel melon chains connected via hydrogen bonds, as found by Lotsch et al. and confirmed in later studies. The unit cell is orthorhombic with the space group $P2_12_12_1$.[63–65] This structure model will be assumed in the following, instead of a graphitic sheet-structure with a defined C/N ratio of 3/4, as implied by the stoichiometry in C_3N_4. Powder XRD patterns of the composites show the reflections for FeS_2 and for V_N-CN (KOH-etched, vacancy-rich). The intensity of the reflections of FeS_2 increases with increasing FeS_2 amounts in the composites (**Figure 1**). No additional phases could be observed. Enlarged and normalized PXRD patterns of V_N-CN and the composites (Figure S2, Supporting Information) show a shift of the (002) reflection at around 27° 2θ toward higher ° 2θ values compared to untreated CN. The shift and a decrease in the intensity upon KOH treatment can be assigned to a decrease in interplanar stacking distance and a general loss of order, which has been ascribed to either introduced cyano groups or nitrogen vacancies.[13,66,67]

For further characterization of the morphology, SEM images and EDX maps were recorded. They show FeS_2 particles in the µm range, distributed all over the V_N-CN matrix (**Figure 2** and Figure S3, Supporting Information). EDX analysis confirmed the particles to be FeS_2 with a ratio close to the ideal value of Fe:S 1:2 (Table S1, Supporting Information) and the surrounding matrix to consist of CN with a C/N ratio of ≈0.52. This is lower than the ideal value of 0.75 and could be an indication of free amino groups in the sample, although it is also effected by the low sensitivity of EDX for light-weight atoms.

Physisorption measurements were conducted to evaluate the surface area of the composites with the BET model (Table S2,

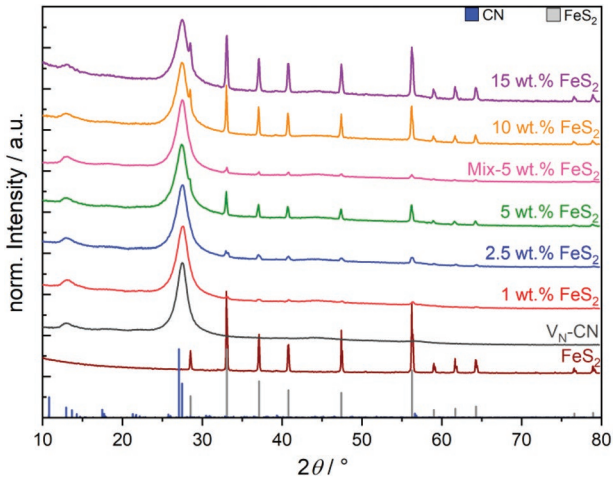

Figure 1. Powder XRD patterns for composites of FeS_2 and V_N-CN and a physical mixture of both constituents (Mix-5 wt%).

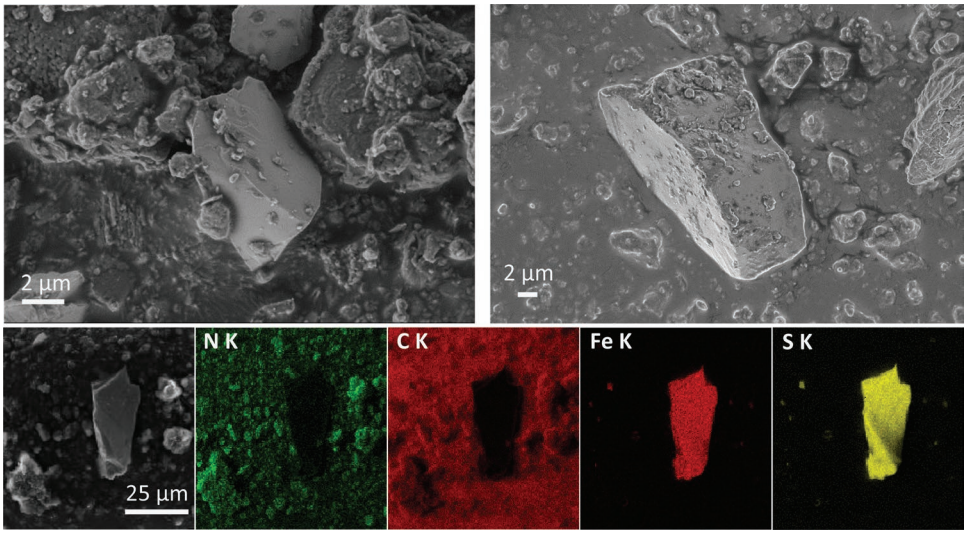

Figure 2. SEM images of a composite of CN and pyrite (5 wt%), clearly showing the distribution of singular FeS_2 particles over CN (top) and EDX maps of a section containing a pyrite particle (bottom).

Supporting Information). Pristine CN exhibits the highest surface area of 10.6 m^2 g^{-1}, which slightly decreases upon KOH treatment. This is in good agreement with the decreased interlayer stacking distance observed in the XRD patterns and otherwise retention of the morphology. The apparent further decrease of the specific surface area upon composite formation can be explained by a difference in material density and particle size between CN and FeS_2.

The optical properties of a photocatalyst are of utmost importance, since they vastly determine the efficiency in light harvesting. The color of the composites gradually gained a tinge of grey with increased FeS_2 content, compared to the previously pale yellow coloring of both untreated CN and V_N-CN (Figure S1, Supporting Information). Diffuse reflectance UV/vis measurements were conducted to elucidate the effect of FeS_2 addition on the absorption behavior (**Figure 3**). CN is an indirect n-type semiconductor.[68,69] Therefore, an indirect Tauc plot was used for a more accurate determination of the band gap and compared to the values apparent in the Kubelka–Munk plots. KOH treatment results in a slight decrease of the band gap of CN from 2.73 to 2.70 eV, and marginally improved absorption in the UV region. The band gap reduction – and thus red-shifted absorption – could be caused by the introduction of cyano groups, whose electron-withdrawing properties were reported to lower the conduction band edge and lead to a narrowing of the band gap.[20,70] The increased UV absorption might be caused by improved charge separation due to the decreased layer distance and the introduction of cyano groups, since transitions in the UV region are commonly ascribed to π-π^* transitions in sp^2 hybridized centers of the aromatic system.[28,71]

The composites exhibit essentially all the same band gap, which is an indication that the major contribution to the light absorption is given by CN. This is expected, since its concentration is much higher than that of FeS_2. Therefore, only changes in the absorption behavior of CN are evaluated from the spectra. The band gap of the composites is slightly increased but very comparable to V_N-CN with a change from 2.70 to 2.78 eV (Figure 3b). The UV absorption of the composites is increased compared to V_N-CN. Both effects hint at a change in the electronic structure and availability of electrons in the π-system. The color change and increased absorption of visible light upon addition of FeS_2 is reflected by diffuse absorption at higher wavelengths, visible in an offset of the baseline (Figure S5, Supporting Information). The effect of band gap widening is especially pronounced for the composites with a FeS_2 ratio of 2.5 to 10 wt% which might indicate optimal charge separation at medium FeS_2 loading. All band gaps derived from the Kubelka–Munk and Tauc plots are summarized in Table S3 (Supporting Information).

DRIFT spectra were recorded to further elucidate possible structure changes upon composite formation (Figure 3c,d). Comparable DRIFT spectra of CN and V_N-CN were recorded, where the broad signal between 3000 and 3600 cm^{-1} can be assigned to O–H and N–H stretching vibrations, underlining the presence of free amino groups that in turn indicate only partial polymerization. The sharp peaks between 1700 and 1200 cm^{-1} belong to stretching modes of C=N and C–N in the heterocycles, as well as bridging units, and the band at ≈808 cm^{-1} can be assigned to the breathing mode of the *s*-triazine units.[27,72,73] Additionally, a band at 2150 cm^{-1} could be observed, that is ascribed to the presence of cyano groups, that appear to be present in CN and V_N-CN as well as in the composites to varying extent.[20,27,73] KOH treatment increases the amount of cyano groups, as well as –OH and/ or $–NH_x$ groups. Additionally, the signals arising from stretching vibrations in the heptazine units are of slightly lower intensity for the defective CN, (relative to the signal at 1720 cm^{-1}), as is the one for deformation vibrations at 808 cm^{-1} (Figure S6, Supporting Information). This is an indication of structural damage inflicted on the heptazine framework, as would be expected by the formation of defects.

The spectra of the composites are fairly similar to that of V_N-CN, indicating retention of the structure. An increased absorbance of the vibration of the heptazine units relative to

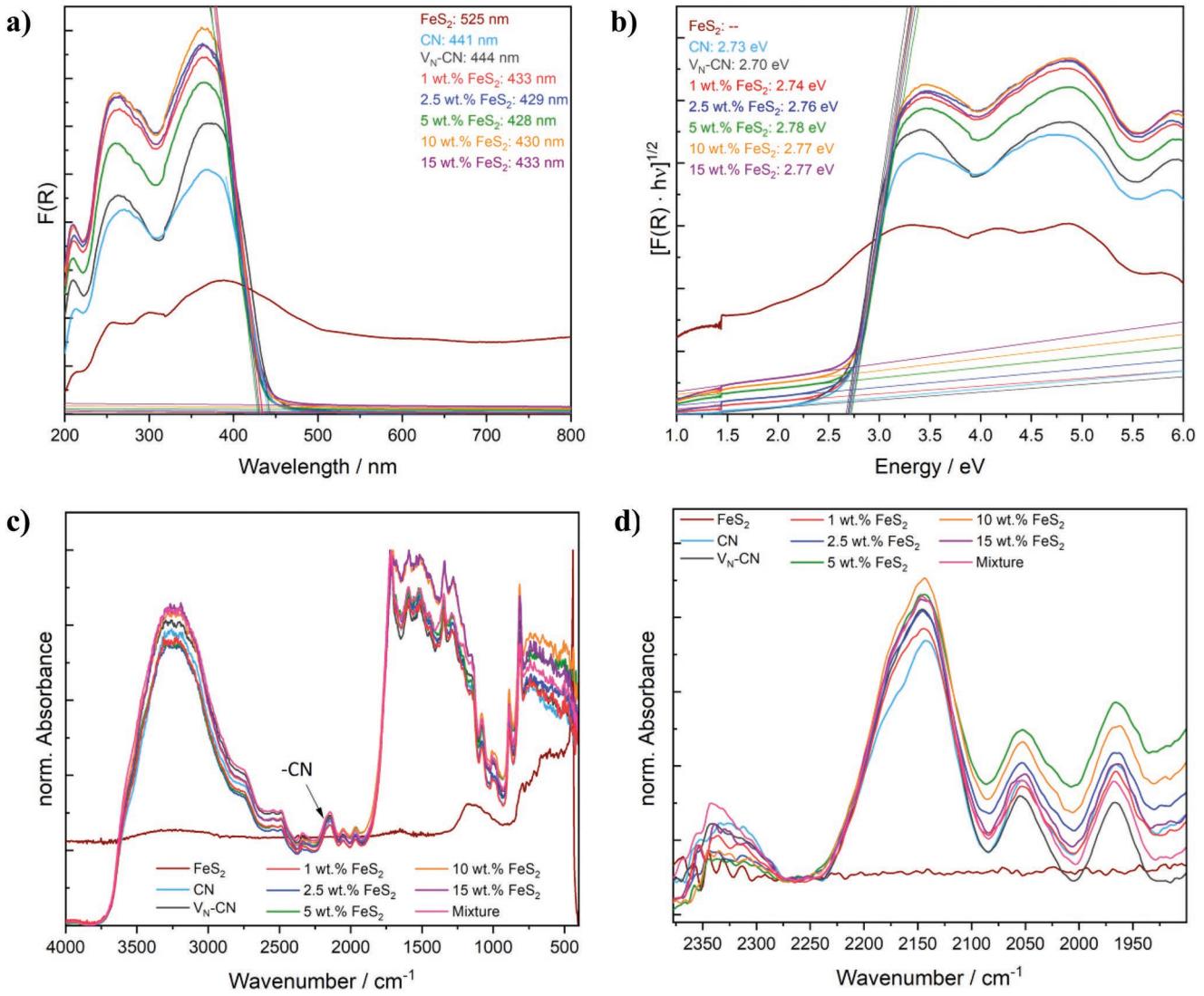

Figure 3. a) Kubelka–Munk and corresponding b) indirect Tauc plot for the composites. c) DRIFT spectra of the composites of FeS_2 and V_N-CN and d) a magnified excerpt for the cyano group vibration.

that at 1720 cm^{-1} was observed for the composites with 10 and 15% FeS_2 in the normalized spectra—an opposite effect to that caused by the KOH treatment. The signals for heterocycle-vibrations at higher wavenumbers (closer to 1700 cm^{-1}) stem from C=N vibrations, while those at lower wavenumbers (closer to 1100 cm^{-1}) arise from C-N vibrations.[74] Therefore, mainly C=N vibrations appear to be affected by the addition of FeS_2. We additionally observe a slight shift of the vibrations for the heptazine unit toward lower wavenumbers, that hints at minor changes in the vibration energy of the entire heptazine framework (Figure S6, Supporting Information).

To further investigate the structural evolutions upon KOH etching and composite formation, XPS measurements were conducted on bulk CN, V_N-CN and a composite containing 5 wt% of FeS_2. Survey scans show the expected signals for carbon, nitrogen and low amounts of oxygen in several spots (Figure S7, Supporting Information). The latter is mainly due to adventitious carbon at the surface and not OH-groups in the defective CN, since oxygen was also observed in several spots on bulk CN. C/N ratios for bulk CN, and V_N-CN, are 0.62 and 0.71, respectively, after correction for adventitious carbon, with slight deviations depending on the measured spot (Table S4, Supporting Information). This is in good agreement to the C/N ratio derived from XPS analysis in literature and with the expected ratio for melon.[75,73] The increased carbon ratio in V_N-CN might indicate the introduction of nitrogen vacancies. The C/N ratio in the composite is with 0.71 identical to that of V_N-CN, underlining that the structure remains intact during composite formation.

Generally, KOH treatment on bulk CN is expected to lead to partial hydrolysis of the structure. Yu et al. proposed a deprotonation of an apex amine group, during thermal polymerization in the presence of KOH which led to a breaking of the topmost cycle of the heptazine unit and cyano group formation. The overall amount of amino groups is retained here.[73] The reaction conditions notably differ from those employed in this

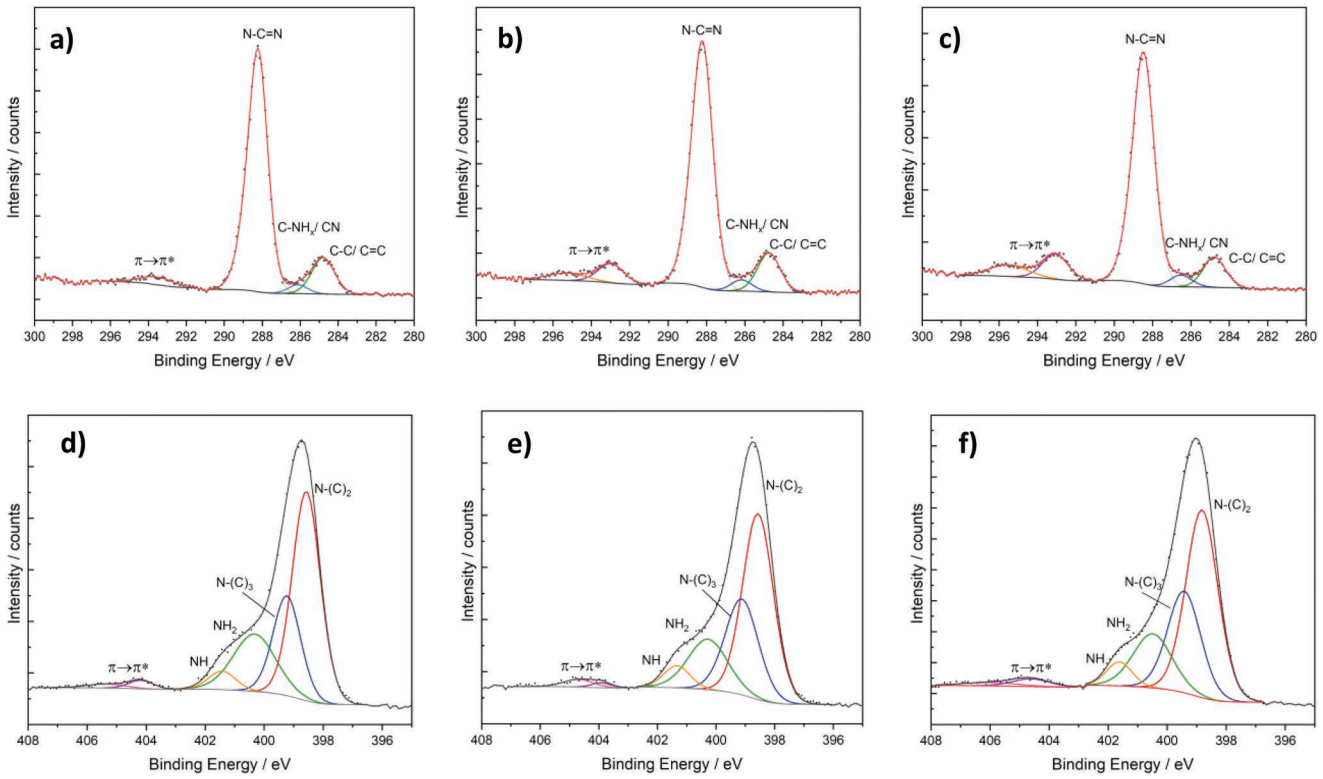

Figure 4. C 1s spectra for a) bulk CN, b) V_N-CN, and c) the composite with 5 wt% FeS_2. Possible fitting of the N 1s spectra for d) bulk CN, e) V_N-CN, and f) the composite containing 5 wt% of FeS_2.

work, but similar structural changes, specifically the introduction of cyano groups in addition to possible vacancy formation, are expected. Nitrogen vacancies are generally believed to be introduced at C–N=C sites.[28] These kinds of possible defects are mainly considered in the following.

Two main peaks are observed in the C 1*s* spectra of CN, corresponding to adventitious carbon at 284.8 eV and N-C=N species in the aromatic system at 288.2 eV (**Figure 4**). The other peak at 281.6 eV can be assigned to carbon adjacent to amino groups.[27,72] Carbon atoms bound to cyano groups are expected to have a similar – though slightly higher – binding energy, that will overlap with this peak.[64,73] A minor shift from 286.1 to 286.2 eV is visible in the spectrum for V_N-CN, hinting at an increase in the amount of cyano groups, as observed in the DRIFT spectra. This is further supported by changes in the ratios of the respective signal to that of C–C and N–C=N. Another effect is the observation of a new π-π^* satellite at 295.3 eV in case of V_N-CN and a growth in the intensity of the π-π^* satellite at ≈293 eV, indicating the presence of larger numbers of free electrons in the vacancy rich system, or more favorable excitation of these. This is in good agreement to the observations from UV spectroscopy and to literature.[28,76] Furthermore, a reduction of the asymmetry of the peak at 288.2 eV upon KOH-treatment indicates damage inflicted on the aromatic system, which is in good agreement with the assumed breaking of some heptazine units. The formation of a composite of V_N-CN and FeS_2 results in a comparable C 1*s* XP spectrum only that the signals of carbon in both the –N–C=N and in the cyano group shift toward higher binding energy (Figure 4 and **Table 1**). This might indicate electron extraction from the entire heptazine framework, resulting in partial oxidation.

Four peaks are identified in the N 1*s* spectra for bulk CN at ≈398.6, 399.2, 401.4, and ≈404 eV, in good agreement to the literature (Figure 4).[27,28,72,73] Correlation of the signals with corresponding nitrogen species is challenging, since peak assignment in the literature is ambiguous.[64] The most prominent peak at 398.6 eV in the spectra for bulk CN, and V_N-CN both can be assigned to –C–N=C species in the heptazine units (marked as N–$(C)_2$ in the following), and a small peak at 404.9 eV corresponds to a π-π^* satellite. The signals between 401 and 399 eV can be attributed to amino groups and to the nitrogen atom in the middle of a heptazine unit (N–$(C)_3$), although the exact assignment of the signals to the two nitrogen species is discussed controversially.[28,64,72,75] Additionally, the signal for amino nitrogen should further be fitted by two, since the structure is not ideally graphitic, but closer to that of parallel melon chains, which results in the presence of both –NH and –NH_2 groups, of which the primary amino group is expected at lower binding energy (Figure 4).[62,64] Cyano groups give rise to a signal at ≈400.1 eV, which is indistinguishable from either the signal for the amino groups, or that of N–$(C)_3$.[64]

Generally, the nature of the N 1*s* spectra allows for the possibility of various fits that give good results mathematically but are meaningless in a chemical and physical sense, due to a large number of independent fitting parameters. This is demonstrated in Figure S8 (Supporting Information). If we assume that the structure of CN obtained via thermal polymerization of melamine lies in between the model of parallel melon chains

Table 1. Binding energy and atomic ratios for different species in the N 1s and C 1s spectra.

		–NH	$–NH_2$	$N–(C)_3$	$N–(C)_2$	$\pi \rightarrow \pi^*$	$N–(C)_2/N–(C)_3$	$N–(C)_2/NH$
CN	Binding energy [eV]	401.4	400.3	399.2	398.6	404.1, 405.3		
	Amount [at%]	4.4	21.1	23.8	50.8		2.13	11.55
V_N-CN	Binding energy [eV]	401.3	400.3	399.1	398.6	404.4		
	Amount [at%]	5.1	17.5	27.8	49.7		1.79	9.75
5 wt% FeS_2	Binding energy [eV]	401.6	400.5	399.4	398.8	404.7		
	Amount [at%]	5.1	17.5	27.8	49.7		1.79	9.75
		C–C	N–C=N	$C\text{-}NH_x$; CN	$\pi \rightarrow \pi^*$	$\pi \rightarrow \pi^*$	CN/N–C=N	CN/C–C
CN	Binding energy [eV]	284.8	288.2	286.1				
	Amount [at%]	14.3	82.7	3.0	293.6			0.21
V_N-CN	Binding energy [eV]	284.8	288.2	286.2	293.0	295.2		
	Amount [at%]	14.0	82.3	3.7			0.045	0.26
5 wt% FeS_2	Binding energy [eV]	284.8	288.5	286.5	293.1	295.6		
	Amount [at%]	11.3	84.4	4.3			0.051	0.38

and of fully condensed sheets, the amount of NH should be smallest, compared to the other nitrogen species.[64] This expectation supports an assignment of the signal at 401.5 eV to NH instead of $N–(C)_3$. Considering, that the signals for primary and secondary amines are likely to be adjacent, we follow assignment of the nitrogen species as: $N–(C)_2$ at 398.7 eV, $N–(C)_3$ at 399.5 eV, NH_2 at 400.5 and NH at 401.5 eV, although we stress that a reverse assignment, as suggested in some XPS studies on pristine CN also has its merits.[64,75] To allow for comparison of the spectra for V_N-CN and the composites with that for bulk CN, we therefore fitted the spectra using several constraints based on structural relationships (Figures S9 and Figure S10, Supporting Information). Further information about the fitting process is given in the Supporting Information.

The binding energies and atomic ratios for both the C 1s and the N 1s spectra with the most reasonable fitting result are summarized in Table 1.

In order to still derive meaningful insights into structural changes from the N 1*s* spectra, despite the variable fitting, we decided on normalization of the spectra (Figure S11, Supporting Information). Two things become immediately obvious. One is a shift of the main peak in the N 1s spectra from 398.7 to 399.0 eV upon composite formation, indicating an increase in the binding energy of $N–(C)_2$ in the heptazine units, as discussed above. Additionally, the "shoulder" at ≈401 eV is pronounced less sharply, indicating larger amounts of nitrogen species at medium binding energy. The same shift toward higher binding energy is observed in the C 1*s* spectra, together with an increased intensity of the $\pi \rightarrow \pi^*$-satellite. The lower amount of cyano groups in the untreated CN is also shown by the lower intensity at 286 eV compared to both V_N-CN and the composite. These observations confirm the main conclusions drawn from the N 1*s* spectra above, without relying on arbitrary fitting results.

Concluding these considerations, XPS analysis supports the introduction of both cyano groups and vacancies upon KOH treatment. Furthermore, it elucidates the changes in the electronic structure upon addition of FeS_2 to the system, indicating partial electron extraction from the V_N-CN matrix. Hydrolysis and introduction of OH-groups similar to what has been observed for hydrothermal treatment with NaOH, involving the breaking of NH-bridging bonds and introduction of OH-groups cannot be totally excluded, but is not likely to have a major influence, since oxygen contents are similar in both CN and V_N-CN.[65]

TGA-MS measurements were conducted on the composite containing 5 wt% of FeS_2 and on both of the constituents, FeS_2 and V_N-CN, to confirm that no structural changes occur during synthesis while thermal treatment for 2 h at 200 °C (Figure S12, Supporting Information). FeS_2 was stable up until about 400 °C, above which a gradual extraction of sulfur in the form of SO_2 was observed. Notably, the lack of an increase in the mass indicates an absence of significant oxidation during the initial heating phase. For V_N-CN, a major mass loss is observed starting at 570 °C, which is completed at around 720 °C. During the heating in synthetic air, NO, H_2O, and CO_2 were found to be the main combustion products up until around 650 °C, after which an increase in the evolution of CO and NO_2 was observed (Figure S13, Supporting Information). The two steps of the combustion process are also apparent in the DSC curves (Figure S12, Supporting Information). The TGA curves for the composite show many similarities compared to that of CN. However, both the mass loss curves and the ion currents for the evolving gasses are shifted by almost 100 °C to lower temperatures, signifying that the presence of FeS_2 boosts the decomposition, likely acting as a catalyst and activating the heptazine units. Nevertheless, the observed thermal decomposition only occurs at temperatures far above the 200 °C, thus precluding decomposition during the composite formation.

The interaction with FeS_2 mainly involves the nitrogen in V_N-CN, as shown in the much decreased ion current for NO_2 during the second step of the combustion process, indicating, that more nitrogen is extracted from the structure in the beginning. This is confirmed by the DSC curves, where the sharp peak at the end of the combustion process is much less pronounced (at 586 and 712 °C, respectively). While the ion currents for all gaseous combustion products in V_N-CN show one signal with a sharp peak current, those of the composites appear as double peaks. Perhaps they correspond to the

combustion of areas in close proximity to FeS_2 and to areas for which the influence of FeS_2 is less. Since the ion currents for both NO and NO_2 are significantly lowered compared to that in CN (also in relation to the ion current for CO_2, so this observation is not only due to the lower content of CN), new nitrogen containing reaction products might be formed, that were not detected.

2.2. Photocatalytic NH_3 Generation

Photocatalysis was performed in a semi-batch setup using 20 vol% of methanol as a hole scavenger. The reaction was investigated for V_N-CN and composites therewith containing different amounts of FeS_2. After the irradiation period of 7 h, the solution was directly filtered and analyzed for NH_3 by the salicylate test. Additionally, the concentration of NH_3 in an acid trap located behind the reactor was evaluated. The calibration curves can be found in Figure S14 (Supporting Information). The quantification of NH_3 was performed after stable color development, which was only obtained after several hours in the dark (Figure S15, Supporting Information).

The decoration of V_N-CN with FeS_2 can significantly enhance the NH_3 yield by a factor of 1.63 from 494 to 801 µg L^{-1}, which equals to 3.9 and 6.4 µmol h^{-1} for 200 mg photocatalyst, respectively. Compared to the untreated CN the activity is enhanced by ≈400%, clearly showing that a combination of defect introduction and interaction with FeS_2 is necessary for efficient ammonia generation. The ammonia yield is comparable for a FeS_2 content between 1 and 5 wt% (**Figure 5** and Figure S17, Supporting Information), although decreasing and dropping significantly for FeS_2 ratios above 10 wt%. Already low amounts of FeS_2 are sufficient for the activation and further loadings decrease the activity due to shadowing effects and a reduced ratio of the active photocatalyst, because FeS_2 itself is inactive in the N_2 reduction, solely yielding H_2 under illumination (Figures S17 and S21, Supporting Information).

Several control measurements were conducted, to elucidate the source of nitrogen and the selectivity of the reaction (Figure 5 and Figure S18, Supporting Information). First, a dispersion of a composite photocatalyst in water/methanol was tested for NH_3 after stirring in the dark. No NH_3 was detected in this case. Secondly, a dispersion of V_N-CN was filtered and tested for NH_3 to exclude amino groups in the photocatalyst interfering with the test. No NH_3 was observed in both control measurements. We also tested a physical mixture of FeS_2 (5 wt%) and V_N-CN for photocatalytic NRR ("Mix 5 wt%"), without performing the grinding and subsequent calcination steps that establish an interfacial contact between the two constituents. The activity was significantly lower than that of V_N-CN itself, due to the lower amount of active photocatalyst and lack of interaction between FeS_2 and V_N-CN (Figure 5). This clearly indicates an enhancement effect in ammonia generation based on a direct contact between FeS_2 and V_N-CN.

Additionally, the photocatalytic reaction for the composite containing 5 wt% of FeS_2 was repeated in an argon atmosphere ("5 wt% – Ar"). A similar activity compared to the reaction in N_2 atmosphere was observed, strongly suggesting that the ammonia generation is not based on N_2 feed gas reduction, but stems from the V_N-CN framework instead (Figure 5).

Literature for NRR over vacancy-rich and cyano-rich CN likewise propose a N_2 conversion pathway following a Mars-van Krevelen mechanism, therefore this observation is not surprising,[28] however significant NH_3 yields for CN in an argon atmosphere, like we show, were not reported. Therefore, the performance of careful blind experiments in combination with detailed material characterization before and after photocatalysis is of high necessity.

The reaction solutions were additionally tested for nitrogen-containing by-products such as hydrazine and NO_3^-. No hydrazine and only trace amounts of NO_3^- around the lower detection limit were found for both V_N-CN, and the composites (Figures S19 and S20, Supporting Information), when the photocatalytic experiment was performed in N_2, but not in an

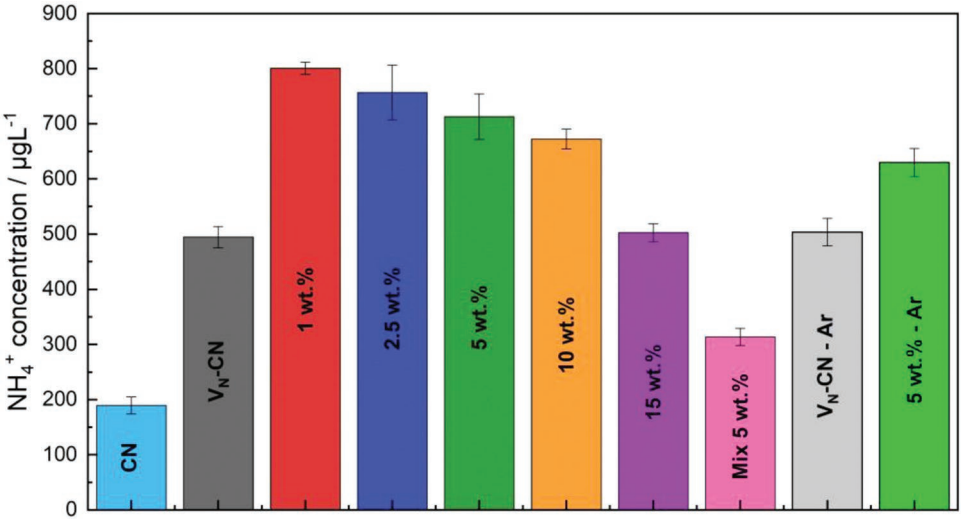

Figure 5. Ammonia concentration after 7 h obtained for composites with a different FeS_2 ratio. The reaction solution was analyzed multiple times for NH_3 and the results were averaged. Additionally, determined concentrations for reference measurement in Ar atmosphere and a physical mixture of FeS_2 and V_N-CN (Mix 5 wt%) are shown.

Ar atmosphere. The main side product was H_2, with a production rate of around 200 µmol h^{-1}. The rate was similar for all composites, with a slightly increased H_2 formation rate for higher amounts of FeS_2 in the sample (Figure S21, Supporting Information). FeS_2 itself showed a remarkably high H_2 production rate of 370 µmol h^{-1}. Thus, both the activity improvement for NH_3 generation and the selectivity are highest for lower FeS_2 loadings in the composites.

A gradual decrease in the H_2 evolution rate over time is in good agreement with a possible Mars-van-Krevelen-type of structural changes during the illumination. When the photocatalytic experiment was performed in an argon atmosphere, similar H_2 evolution rates were observed as compared to the results in a N_2 atmosphere (Figure S21, Supporting Information).

In order to elucidate the formation of methanol oxidation products, UV absorption spectra of the reaction solutions were recorded after the photocatalytic experiments. Critical evaluation of the conditions and evolving organic oxidation products is crucial, since the accuracy of the salicylate test can be influenced by a variety of parameters that are too often not considered. There is a correlation between the amount of NH_3 produced and the amount of UV light absorbance by the filtered reaction solutions at 205–220 nm (**Figure 6**). This absorbance can mainly be attributed to formic acid that is formed alongside NH_3 (Figure S22, Supporting Information). This could have an effect on the salicylate test, resulting in a significant underestimation of the actual NH_3 concentration.[77] For this reason a 12 % hypochlorite solution was used, which negates the effect of varying acid generation. Additionally, a reference sample of known ammonia concentration was always measured together with the reaction solution to avoid errors based on the testing solutions. All concentrations given in the paper are averaged between several quantification measurements with the salicylate test.

Additionally, the spectra clearly show the presence of other ions that absorb UV-light, which is even more obvious in the derivation spectra (Figure S23, Supporting Information). The overlap of multiple features renders an accurate identification nearly impossible, however. Nitrate and nitrite absorb UV light at 203 and at 210 nm, respectively.[78] No clear absorption feature could be identified for nitrite, while a very small contribution of nitrate might be discernible for V_N-CN and composites thereof, which is in good agreement to the results from ion chromatography. The absorption peak at 220 nm probably stems from π–π^* transitions, possibly in carbonyl groups of amides or very short conjugated systems.[79] The broad absorbance from 230 nm toward higher wavelengths could in part be caused by very fine FeS_2 particles, since a filtered FeS_2 dispersion gives rise to a noticeable absorbance signal up to 450 nm (Figure S22, Supporting Information).

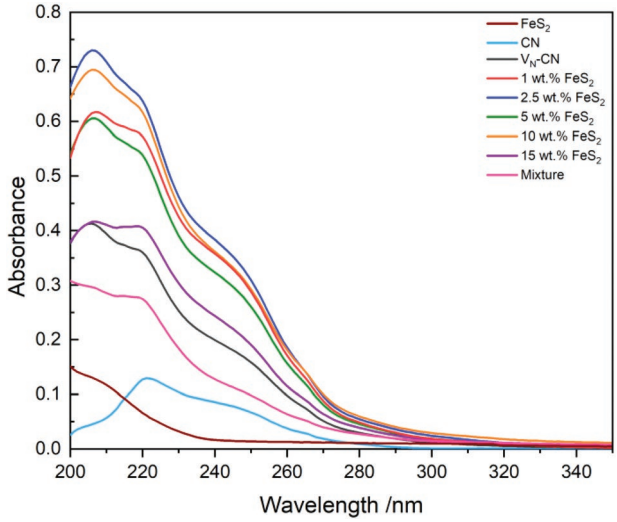

Figure 6. UV spectroscopy for the filtered reaction solutions after the NRR experiments.

To exclude significant errors in the determined ammonia concentration due to the large amounts of organic byproducts, the solutions were measured with ion chromatography and the values compared to those from the colorimetric determination (**Table 2**). The general trend is the same as observed with the salicylate tests, but the determined ammonia concentrations are slightly higher. This is to be expected, since the significant amounts of methanol and formed formic acid largely affect the colorimetric test, resulting in an underestimation of the actual ammonia concentration, and even with careful optimization of the testing procedure, some influence of the organic substances cannot be avoided. A graphic depiction of the concentrations determined with ion chromatography, as well as an exemplary chromatographic trace can be found in Figure S24 (Supporting Information).

Since hardly any difference in the NH_3 yield in argon and N_2 atmosphere was observed after 7 h for the most active sample, we devised a longtime measurement. A dispersion of the composite containing 5 wt% FeS_2 was first illuminated for 14 h in either N_2 or argon atmosphere. Every two hours, a sample was taken and analyzed for NH_3. After 14 h, the lamp was switched off and the solution was stirred in the dark for 6 h under continuous gas flow of the respective gas, before illumination was continued for another 6 h (Figure S25, Supporting Information). During the first irradiation period, the generated amount of NH_3 increased almost linearly with a rate of ≈82 µg h^{-1} in N_2 and 90 µg h^{-1} in argon atmosphere, respectively. Once the

Table 2. Ammonia concentrations determined with the salicylate test and with ion chromatography.

Sample	Ammonia concentration determined with the salicylate test [µg L^{-1}]	Ammonia concentration determined with ion chromatography [µg L^{-1}]
FeS_2	–	6.8 ± 5.7
CN	189.4 ± 15.5	308.7 ± 8.0
V_N-CN	494.2 ± 19.1	832.5 ± 28.4
1 wt% FeS_2	800.7 ± 11.3	1188.3 ± 1.4
2.5 wt% FeS_2	756.7 ± 49.6	1173.6 ± 30.5
5 wt% FeS_2	712.7 ± 41.4	1138.1 ± 17.4
10 wt% FeS_2	672.2 ± 18.0	1086.5 ± 11.3
15 wt% FeS_2	502.3 ± 16.5	812.0 ± 6.2
Mix	313.5 ± 15.5	508.7 ± 14.3
V_N-CN-Ar	503.4 ± 24.8	775.5 ± 2.4
5 wt% FeS_2-Ar	629.6 ± 25.5	948.3 ± 39.0

Table 3. Quantum Yield at 355 nm for the composites containing different amounts of FeS_2.

	V_N-CN	1 wt% FeS_2	2.5 wt% FeS_2	5 wt% FeS_2	10 wt% FeS_2	15 wt% FeS_2
355 nm	12.0%	6.6%	6.7%	6.1%	6.2%	4.3%

lamp was switched off, the measured concentration slightly decreased in both atmospheres, likely due to NH_3 carried out of the reactor by the gas flow. After continuing the light irradiation, the NH_3 generation was increased again with about the same rate, as before the period in the dark. Afterward, the determined concentrations seem to level out. This effect is likely caused by a combination of slow degradation of the structure and accumulation of oxidation products. A similar effect was observed for the H_2 evolution rate, indicating that the observed effect is not solely caused by the accumulation of formic acid (Figure S25b, Supporting Information).

In addition to the NH_3 concentration reported in the reaction solution, NH_3 was detected in the acid trap but not included in the concentrations given here. The amounts of NH_3 were maximum around 6.5 µg and 3.5 µg total for the experiments in an argon and a nitrogen atmosphere, respectively (Table S8, Supporting Information). Still, the use of an acid trap is sensible. The pH of a dispersion of 20 mg of V_N-CN in 20 mL of H_2O was ≈9.5. Thus, both NH_4^+ and NH_3 species can occur in significant amounts. For CN the pH is with ≈8 closer to neutral, perhaps due to higher amount of imine or amine groups in V_N-CN. A slightly alkaline pH for CN is expected, due to the large number of amino groups.

2.3. Post-Photocatalytic Characterization

Both V_N-CN and the composites with FeS_2 were thoroughly characterized after the photocatalytic experiments, in order to evaluate the stability and to gain further insights into the ammonia generation pathway. Post-photocatalytic XRD patterns still show the same reflections for phase-pure CN and FeS_2 (Figure S26, Supporting Information). The intensity for the FeS_2 reflections is significantly decreased after the NRR. This effect could be a result of a loss of interfacial contact between FeS_2 and CN as verified by dispersing a composite in water/methanol mixtures and subsequently regaining the material via centrifugation (Figure S27, Supporting Information). FeS_2 is known for its flotation tendency in mineral separation, due to its relative hydrophobicity.[80] Additionally, we tested the stability of FeS_2 during both the formation of the composite (with annealing at 200 °C) and storage of the sample in air. No changes in the crystal structure of FeS_2 were observed (Figure S27, Supporting Information).

UV/vis spectra show a significantly increased absorbance of UV light and a decrease of the band gap (Figure S28, Supporting Information). Both V_N-CN and the composites showed a pronounced darkening after the NRR that decreased again after storage in air (Figure S29, Supporting Information). The effect of increased UV light absorption is less obvious for the composite containing 15 wt% compared to the other composites, for which the activity was also lowest. All other composites that exhibited a similar activity, show a similar increase in UV absorption, which likely correlates to higher degrees of structural change. The increased UV absorption is less pronounced for V_N-CN in agreement with the lower activity. The band gap decreases very slightly by 0.03 eV for V_N-CN. For the composite containing 5 wt%, the decrease is most drastic and the band gap is experiencing a change by 0.07 eV from 2.78 to 2.71 eV. The red shift of the absorption might be caused by defect formation and distortion of the structure.[81]

DRIFT spectra of the composites after the NRR experiments show a marked decrease in the vibrations for the heptazine units (Figures S30 and S31, Supporting Information), especially in relation to the vibration at 1720 cm^{-1}, that falls into the range for C=N vibrations. This vibration is further shifted back to slightly higher wavenumbers. A decrease in the relative intensity of the 808 cm^{-1} vibration agrees with this observation, indicating structural damage to the heptazine framework. Both effects were also observed to a lesser extent upon introduction of vacancies and cyano groups upon KOH treatment and thus confirm further breakdown of the heptazine units during photocatalysis. Additionally, a closer look at the vibration at 2147 cm^{-1} reveals a decrease in the intensity, supporting the assumption that cyano groups are consumed during the photocatalytic experiment (Figure S32, Supporting Information). The effect is even more increased for long-term experiments, highlighting the further degradation of cyano groups with prolonged illumination times (Figure S32, Supporting Information).

XP spectra of the composite containing 5 wt% of FeS_2 after the photocatalytic reaction show a slight shift for the carbon species adjacent to cyano-/amino-nitrogen and the N–C=N peak toward lower binding energies (Figure S33, Supporting Information). The intensity for both peaks in the C 1*s* spectra corresponding to the V_N-CN structure decreases markedly in relation to that of C–C, further indicating structural changes, that do not only extend to nitrogen, but are further inflicted on carbon in the structure. The ratio might also partly be influenced by adsorbed organic residues from the sacrificial agent. Additionally, the intensity for the satellite peaks is decreased, supporting damage to the aromatic system. The calculated C/N ratio from the survey scan was 0.88, without correction for adventitious carbon, because the amount of C–C or C=C bonds possibly present in the structure after partial extraction of nitrogen is unknown. Thus the C/N ratio is increased compared to 0.80 for the same composite before the photocatalytic experiment. This is a strong indication of nitrogen extraction from the V_N-CN matrix.

Sample composition was additionally evaluated by elemental analysis before and after photocatalytic experiments (Figure S34, Supporting Information). The amount of sulfur and thus probably also FeS_2 was noticeably decreased after the photocatalytic experiment for all composites. This is likely an effect of the imperfect interfacial contact and washing of the sample, as has already been observed in the XRD patterns.

For a more detailed comparison, the C/N ratio was calculated for the composite samples before and after the photocatalytic reaction. For all composites, the C/N ratio was about 0.555, which significantly differs from the compositional value of 0.75 and indicates incomplete polymerization and the existence of

many free amino groups. The value is in good agreement to the EDX measurements, though. No significant differences of the C/N ratio were observed for different FeS_2 loadings. For all composites, the C/N ratio was visibly increased after the photocatalytic reaction, supporting the extraction of nitrogen from the structure (Figure S34, Supporting Information). Compared to the C/N ratios obtained from XPS measurements, the nitrogen content in the bulk is significantly higher, due to adsorbed carbon impurities and possibly nitrogen deficiency at the surface. Elemental analysis additionally shows an increase in the C/N ratio after the KOH treatment, supporting the generation of nitrogen vacancies (Figure S34c, Supporting Information). Based on the difference in the C/N ratio of 0.005 for V_N-CN, an extracted nitrogen fraction of 0.94% can be estimated. For further information about the calculations see the Supporting Information.

2.4. Charge Carrier Dynamics

Due to the large variety of defects that can potentially be present in V_N-CN, the electronic structure is rather complex and should be studied in detail, in order to get explanations for the different results in photocatalytic experiments. To investigate the charge carrier dynamics, transient absorption spectroscopy (TAS) in diffuse reflectance geometry was employed. In **Figure 7** the ns-TAS measurements of a composite of V_N-CN and 5 wt% of FeS_2 in an argon atmosphere are presented. The positive absorption feature between 650 nm and 900 nm can be assigned to photogenerated electrons in V_N-CN.[81–84] The same signal is generally apparent in the measurement of the composite, but an increase of the relative absorption intensity in the range between 650 and 750 nm is noticeable, in comparison to the main signal between 750 and 900 nm. This might indicate a change in the electronic structure upon composite formation with FeS_2 and an increased relative amount of photogenerated electrons in an additional excited state, which possibly corresponds to an intraband gap state caused by defects. For a better comparison the main signal of the photogenerated electrons in both materials was analyzed regarding the lifetime of these electrons. The lifetimes monitored at 800 nm for both V_N-CN and the composite are comparable and in the order of ns (Figure S35, Supporting Information). The signal is best fitted with two different lifetimes, that are 3.4 and 59.0 ns for V_N-CN and 4.3 and 31.7 ns for the composite, respectively.

The shorter lifetime of the electrons is comparable for both materials and could be explained with the fast recombination of charge carriers in the materials. Electrons with fast recombination rates, such as those corresponding to lifetimes of 3–4 ns, can generally not participate in photocatalytic reactions, as they do not reach the surface.[85] The main pathway for exciton separation is between sheets along the stacking direction, for which a hopping rate in the order of 10^9 s^{-1} is assumed, preventing efficient transport to the surface in the short lifetime of only a few nanoseconds.[86] The other lifetime for the composite indicates that the introduction of FeS_2 to the V_N-CN matrix results in the prevention of electron accumulation in deep traps.[81,87]

We additionally used photoluminescence (PL) spectroscopy to gain insights into the radiative energy relaxation levels of the excited photocatalyst. The most dominant PL emission in semiconductors is the band gap emission, where the excited states (charge carriers) recombine and relax to the ground state by emitting radiation. Thus, low PL emission is often an indicator for efficient charge carrier separation and low recombination rates. CN as a polymeric material with a structure in between that of molecules and solid crystals, generally exhibits a prominent blue fluorescence, that has been shown to be significantly influenced by the introduction of defects.[88,89]

Upon irradiation at wavelengths with a higher energy than that of the band gap, a broad fluorescence signal between 410 and 640 nm is observed for V_N-CN and the composites, with a maximum emission at 470 nm and a slightly less intense emission

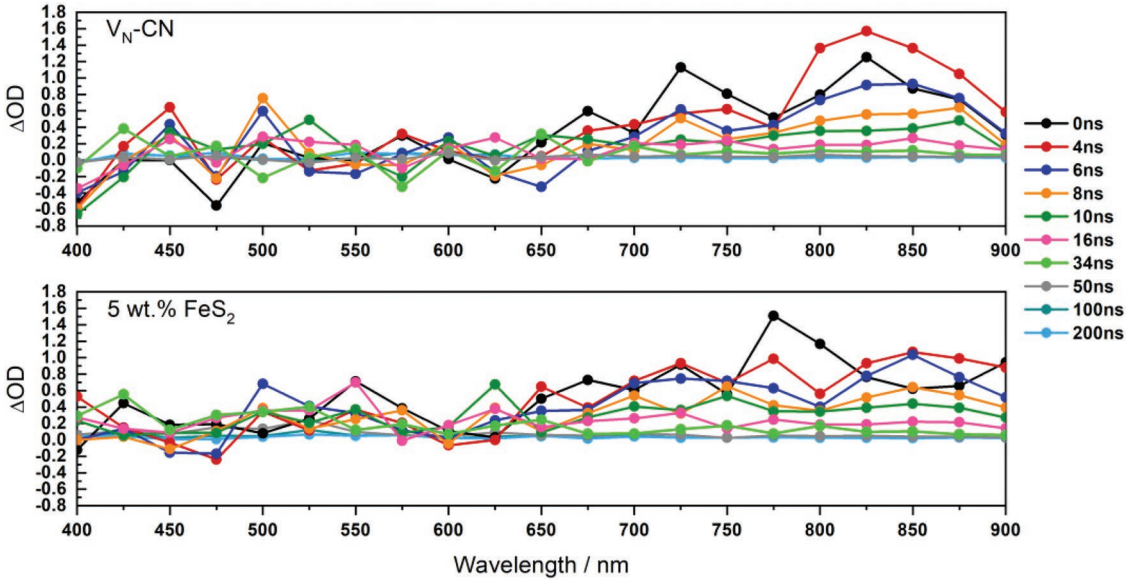

Figure 7. ns-TAS measurements of V_N-CN (top) and the composite containing 5 wt% of FeS_2 (bottom) in argon. Excitation: 355 nm. Connecting lines are only for guiding the eye.

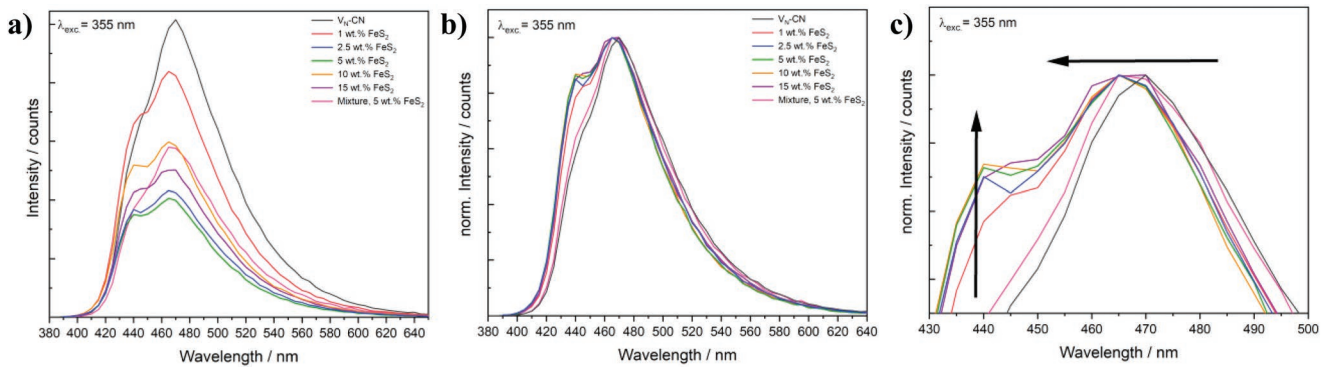

Figure 8. a) Fluorescence emission spectra for the composites for $\lambda_{exc.}$ = 355 nm, b) normalized emission spectra for $\lambda_{exc.}$ = 355 nm, and c) excerpt of the normalized spectra.

at 445 nm, as shown in **Figure 8**. Generally, the fluorescence emission of the composites is decreased compared to V_N-CN, indicating better charge separation and thereby reduced recombination. The photoluminescence is shifted to lower wavelengths for the composites, which is in good agreement to the slightly increased band gaps and indicates a decrease in interlayer electronic coupling.[82,90] FeS_2 itself does not show any fluorescence emission.

The intensity for the emission at 445 nm in relation to that at 470 nm is clearly increased for the composites (Figure 8). The emission at 445 nm can be attributed to direct band gap emission, which is in good agreement to the band gap energy determined via absorption spectroscopy.[81,91] Emission at 470 nm corresponds to transitions from intra band gap states, likely involving lone electron pairs at N–$(C)_3$ sites.[92] An additional tail toward higher wavelengths includes contributions from defect emissions, such as transitions from lone pair states of nitrogen atoms in the *s*-triazine unit, from amino groups, NH-bridging units, or possibly graphitized areas at even higher wavelengths above 500 nm.[88,89] The significantly decreased intensity of lone pair and defect emission in relation to direct band gap emission in the composites, coupled to fluorescence quenching might indicate the inhibition of radiative recombination at defect sites, likely due to interaction of V_N-CN with FeS_2 involving free electron pairs. Since N–$(C)_3$-sites are also effected, the interaction with iron influences the entire electronic structure of V_N-CN, as also observed in DRIFT and XPS measurements. Charge transfer might assist in exciton separation and retard recombination.

The excitation maximum for V_N-CN is located at ≈320 nm which corresponds to band gap transitions (Figures S36 and S37, Supporting Information).[92] The ratio of emission intensity at 320 nm excitation to emission intensity at 380 nm excitation in the normalized excitation spectra is significantly decreased for the composites compared to V_N-CN, along with a slight red-shift of the entire emission signal. The group of Gan et al. ascribes excitation at around 380 nm to transitions from the valence band to lone pairs of –N–$(C)_3$ species, that appears to be more favored for the composites.[92] The absolute emission intensity is decreased at higher wavelengths, since the light absorption is diminished (Figure S37, Supporting Information).

The lifetime of an emission is regarded as a more reliable parameter for judging charge recombination rates. The lifetime was measured for both detection at 445 and 470 nm (Figure S38, Supporting Information). The decay can be fitted with three exponential functions, as is usually done in literature, as well.[14,88] The fluorescence lifetimes are increased again, for the composites, compared to V_N-CN (Table S10, Supporting Information).

The shortest lifetime (τ_3 for emission at 445 nm/τ_3' for emission at 470 nm) for both the composites and V_N-CN, respectively, can be attributed to recombination in the aromatic system.[66] An increase in the second lifetime, τ_2, for the composites compared to defective CN implies improved intraplanar and intrachain charge separation (Figure S39, Supporting Information).[66] This might be due to polarization of the heptazine framework and electron transfer. The greatest difference is observed in the time constants for τ_1, which can be attributed to charge separation between layers (along the π-stacking direction). This is the main pathway for charge separation in carbon nitride.[86] Hence, charge separation in the π system is significantly improved again by FeS_2, affecting both the direct band gap emission at 445 nm and the emission of lone pairs of ternary nitrogen species at 470 nm. The lifetimes are fairly similar for all composites. Fluorescence decay is longer at 470 nm compared to at 445 nm for all samples, supporting the assumption of the main emission at 470 nm mainly being caused by recombination at defect sides (involving free electron pairs of nitrogen species).

The quantum yield (QY) was determined at an excitation energy of 355 nm, to ensure that the increased fluorescent lifetimes truly correlate with improved charge carrier separation. The QY is decreased in the composites with increasing FeS_2, implying that radiative recombination is indeed reduced in the composites (**Table 3**).

2.5. Discussion of the Interaction of FeS_2 and V_N-CN Resulting in Enhancement of Ammonia Generation

Based on the observations for structural changes in V_N-CN induced by the presence of FeS_2, we propose an activation of the structure of V_N-CN by FeS_2. Since KOH treatment is supposed to introduce defect sites that have two nitrogen species with free electron pairs in the vicinity (imine-type nitrogen in =N-CN units and amino groups),[73] an interaction similar to

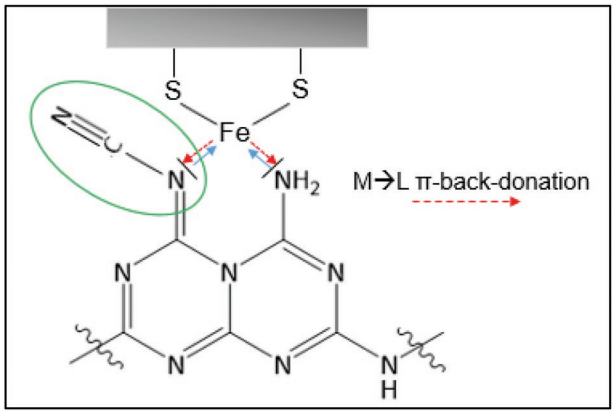

Figure 9. Proposed coordination of nitrogen lone pairs to Fe^{2+} at defect sites and π-back-donation from iron to the nitrogen species, thereby increasing the electron density in the π^* orbitals of the aromatic system and activating the =N-CN group.

ligand to metal coordination to Fe^{2+} appears to be feasible, that results in an activation of the CN structure via π-back-donation and possibly light induced metal to ligand charge transfer (**Figure 9**).

This model is based on following observations:

1) Increased UV absorbance observed for the composites (more π-π^*-transitions) (Figure 3).
2) Band gap widening upon FeS_2 addition (Figure 3): possibly due to deformation/ polarization of the structure upon coordination of defects in V_N-CN to iron centers due to partial electron transfer (σ-Donor) to FeS_2.
3) The shift of both nitrogen and carbon binding energies toward higher values suggests partial oxidation of the structure, thus supporting the σ-donor effect (Figure 4).
4) The increased satellite peaks in the XP spectra suggest higher number of electrons in the π-system, which might be due to π-back-bonding, (Figure 4). Possibly, coordination of the cyano groups and/ or amino groups to Fe^{2+} centers induces a marked electron withdrawing effect and partial charge transfer to iron, reducing the electron delocalization.
5) Fluorescence quenching and decreased QY indicate improved charge transfer (Figure 8 and Table 2).
6) Decreased ratio of emission from lone electron pair states in fluorescence measurements (Figure 8) indicates electronic interaction of defects in V_N-CN with FeS_2.
7) Increased fluorescence lifetime, τ_1, for the composite (Table S10, Supporting Information): electrons in the π-system might be influenced and stabilized by the interaction with iron.
8) An additional signal for photogenerated electrons in the TAS measurements upon composite formation with FeS_2 might arise due to complex interactions of defect states with iron centers, such as light-induced M→L-charge transfer (Figure 7).
9) TGA curves show a shift in the decomposition of V_N-CN promoted by FeS_2, indicating structure activation by FeS_2 (Figure S12, Supporting Information).
10) Shift of the vibration energy to lower values for the heptazine units additionally indicate structure activation: signals for C=N vibrations are apparently more influenced by the FeS_2 addition than C-N vibrations, with the relative intensity decreasing (Figure S6, Supporting Information).
11) π-back-donation from Fe-centers to imine bonds are known, as is back-donation and charge transfer with cyano group.[93,94]
12) The oxidation products in the photocatalytic reaction are the same for both, composites and V_N-CN, (Figure 6), suggesting oxidation on V_N-CN.
13) The HER activity is decreased for the composites (Figure S21, Supporting Information), even though FeS_2 is present, indicating that electrons in FeS_2 are used for other redox reactions, such as π-back-bonding and/or re-oxidation of Fe^{3+} to Fe^{2+}.
14) Slightly enhanced ammonia generation was also observed for untreated CN decorated with FeS_2 (Figure S40, Supporting Information) and was expected due to minor defects in CN (cf. DRIFT results). This further underlines the boosting effect in ammonia generation, when FeS_2 and highly defective, KOH-treated CN are present.
15) Interaction of the composite with N_2 is indicated in the TGA-MS measurements, due to coordination to Fe^{2+}. Such an effect could be advantageous for re-incorporation of nitrogen into the structure.

A control experiment in 100% of methanol yielded comparable ammonia yields in both N_2 and argon atmosphere, underlining again, that the nitrogen is extracted from the carbon nitride framework and not – at least not completely – replenished. It also highlights, that the degradation is not of oxidative nature but inherent in the reduction mechanism (Figure S41, Supporting Information)

3. Conclusion

We have shown that a combination of defect introduction into CN and subsequent composite formation with FeS_2 can significantly improve the amount of ammonia generated in photocatalytic NRR experiments, resulting in four times higher ammonia yields under illumination compared to unmodified CN. The optimal FeS_2 loading was established to be 1 to 5 wt%. The system only employs inexpensive, earth-abundant and non-toxic materials. However, knowledge about the exact structure of CN and the presence and character of defects proved to be crucial, as they significantly influence the interactions between the two constituents. Charge transfer between FeS_2 and V_N-CN was established to proceed at the defect sites, resulting in an electronic activation of the structure. Therefore, NH_3 generation was found to occur not photocatalytically from N_2, but rather via a novel activation route of V_N-CN, involving reduction of the =N-CN group adjacent to nitrogen vacancies. A replenishment of nitrogen in the structure could, however, not yet be verified. FeS_2 acts similar to a cocatalyst, enhancing the ammonia generation, although the process is different to that of (metal) electrocatalysts typically employed for photocatalytic HER or OER. Here, π-back-donation from Fe-centers to imine nitrogen and amino groups of the defect-rich CN reduces the activation barrier for the reduction of terminal cyano groups upon illumination.

Although there are numerous reports on CN for the photocatalytic NRR, the complexity of the system, with a broad variety of defects that can theoretically be present, necessitates a strict control of the synthesis parameters and thorough characterization experiments. We deduce that photocatalytic ammonia generation with defective CN is most likely always a product of self-degradation, which can be enhanced by back-donation with suitable coordinating materials.

4. Experimental Section

Material Synthesis and Characterization: CN was prepared via thermal polymerization of melamine.[95] 1 g of melamine (Sigma Aldrich, 99%) was calcined at 550 °C for 4 h in a closed crucible in air, using a heating ramp of 5 K min^{-1}. The synthesis was repeated several times and the obtained CN powder was ground and thoroughly mixed, before it was used for further modifications and composite formation.

Vacancy-rich CN (V_N-CN) was obtained by dispersing 2 g of the as-synthesized CN in 36 mL of 1 M KOH for 3 h under stirring. Subsequently, the material was collected via centrifugation and washed until neutral with ultrapure water.[25]

For the composite formation, respective amounts of commercial FeS_2 (Sigma Aldrich, 99.8%, 325 mesh) and V_N-CN were ground for 10 min in a mortar, under addition of low amounts of *i*-propanol (p.a.). Subsequently, the mixture was subjected to heat treatment for 2 h at 200°C in air, to improve interfacial contact.

The composites were analyzed before and after the photocatalytic experiments. *Powder X-ray diffraction* (XRD) was measured on a Malvern PANalytical Empyrean device with Cu K_α irradiation (λ_1 = 1.5406 Å; λ_2 = 1.54443 Å). Acceleration voltage and emission current were set to 40 kV and 40 mA, respectively. Peak assignment was performed with X'Pert Highscore plus. Following reference cards were used for the reflection assignment in FeS_2 and FeS, respectively: 00-042-1340, 00-023-1123. The diffraction pattern for CN was calculated with Vesta, using crystallographic data from the group of Irvine.[62]

Diffuse-reflectance UV/vis spectra were obtained using a Perkin Elmer Lambda 750 spectrometer with a Praying Mantis (Harrick) and spectralon as white standard. The Kubelka–Munk function was used for the calculation of pseudo-absorption, $f(R)$.[96] $f(R) = \frac{(1-R)^2}{2 \cdot R}$.

For band gap determination, a Tauc plot was used.[97] $[f(R) \cdot (h\nu)]^{\frac{1}{n}}$ with $n = 0.5$ for direct band gaps and $n = 2$ for indirect ones.

For *diffuse reflectance infrared Fourier transformed spectroscopy* (DRIFT) a Bruker Alpha II spectrometer and the software OPUS were used. Sample scans were taken from 400 to 4000 cm^{-1}, with a resolution of 4 cm^{-1}.

Fluorescence measurements were conducted on a FluoTime 300 spectrometer from PicoQuant, with the software EasyTau2. Emission spectra were recorded at different excitation wavelengths from a 300 W Xe lamp at room temperature in air. Time correlated single photon counting (TCSPC) spectra were measured using 355 nm laser excitation. The software EasyTau2 was employed for fitting of the decay curves, using a tailfit with three exponentials, according to

$$\mathrm{Dec}(t) = \sum_{i=1}^{n_{exp}} A_i e^{-\frac{t}{\tau_i}} + Bkgr_{\mathrm{Dec}} \quad (1)$$

For steady state measurements, the sample was placed in a holder for solid powder samples. For quantum yield (QY) measurements a thin film on the inside of a cuvette was prepared. The cuvette was placed in an integrating sphere. Measurements were conducted for "out" geometry – meaning that the film was positioned outside of the direct excitation path. For the calculation of the quantum yield, the intensity of the fluorescence emission was integrated, and the area A_S was divided by the total integral excitation intensity as measured in an empty reference cuvette (A_{BE}) minus the excitation intensity that is not absorbed by the sample, A_{SE}

$$QY = \frac{A_S}{A_{BE} - A_{SE}} \quad (2)$$

X-ray photoelectron spectroscopy (XPS) was performed with a Physical Electronics PHI VersaProbe III Scanning XPS Microprobe device. Monochromatic Al Kα X-ray irradiation with a beam diameter of 100 µm was used, with the beam voltage being set to 15 kV and X-ray power to 25 W. The sample surface was precleaned by argon cluster sputtering with a gas cluster ion-beam. To avoid surface charging, samples were continuously flooded with slow-moving electrons and Ar^+. For survey scans, pass energy and step size were set to 224 and 0.4 eV, respectively. High-resolution spectra were measured with a pass energy of 26 eV, a step size of 0.1 eV and a step time of 50 ms. For data analysis a CASA XPS 2.3.17 software was used. The background was corrected using Shirley subtraction. Peak fitting was done with Gaussian-Lorentzian line shapes, with 30% Lorentz ratio. For charge correction C 1s was set to 284.8 eV.

Transient absorption spectroscopy data was collected in diffuse reflectance geometry with an LP980 spectrometer (Edinburgh instruments). Pump laser pulse excitation was set at 355 nm (third harmonic of an Nd:YAG laser produced by Ekspla, NT340), while for the probe pulse a 150 W xenon arc lamp was used. Prior to the measurements the powder sample was filled in a cuvette, stored under Argon and sealed directly before the measurement. TAS data was normalized and decays were fitted with exponential decay functions.

N_2 *physisorption measurements* were conducted on a Quadrasorb Evo device from Anton Paar QuantaTec at 77 K to determine Brunauer–Emmet–Teller (BET) surface areas, using the software ASiQwin for data evaluation. Samples were degassed for 12 h at 120 °C prior to measurements. Due to the small surface area, Kr at 77 K was used for FeS_2, in an AS-iQ-MP-MP-AG instrument from Anton Paar QuantaTec.

CHNS *elemental analysis* was performed with an Unicube instrument from Elementar, using sulfanilamide as standard. Approximately 2 mg of the respective sample were weighed into a tin boat, sealed and combusted at temperatures up to 1143 °C in an oxygen/argon atmosphere.

Thermogravimetric Analysis (TGA) with gas evolution detection via mass spectrometry (MS) was conducted with a Netzsch Jupiter STA 449C thermobalance together with a Netzsch Aeolos QMS 403C quadrupole MS, heating the sample at a rate of 5 K min^{-1} up to 900 °C in synthetic air.

Scanning electron microscopy (SEM) images were recorded on a Zeiss Leo 1530 device with an acceleration voltage of 3 kV after sputter-coating with platinum (Cressington Sputter Coater 208 HR). *Energy dispersive X-ray diffraction spectroscopy* (EDX) measurements were conducted on the same instrument, using and an acceleration voltage of 20 kV. An ultra-dry EDX detector by Thermo Fisher Scientific NS7 was employed.

Photocatalysis: Light-induced ammonia generation was performed in a semi-batch setup using a doped Hg immersion lamp (Z4, 700 W Peschl Ultraviolet) placed in a water-cooled quartz-glass inlay and operated at 350 W. 200 mg of the photocatalyst were dispersed in ≈30 mL of water by ultrasonic treatment for 10 min. The dispersion was transferred to the glass reactor and diluted to 600 mL by the addition of water and methanol. The total amount of methanol was 20 vol%. Nitrogen was bubbled through the stirred dispersion at a flow rate of 50 mL min^{-1} overnight to flush out residual air. For prepurification of the inlet gas stream, it was first passed through a 0.1 M $KMnO_4$ solution, followed by a 0.1 M KOH.[8] The dispersion was illuminated for 7 h, during which a constant temperature of 10 °C was ensured by cooling the reactor with the help of a cryostat (Lauda Proline RP845). Evolving gasses were passed through an acid trap containing 10 mL of 1×10^{-3} M H_2SO_4,[98] dried and subsequently analysed by a quadrupole mass spectrometer (HPR-20 Q/C, Hiden Analytical). After the reaction, the dispersion was immediately filtered and tested for NH_3 using the salicylate test method, a modification of the indophenol blue method.[99,100] For the control

experiment in an inert gas atmosphere, an Ar flow of 100 mL min^{-1} was used.

For the salicylate test, a stock solution of sodium hypochlorite and a stock solution containing the catalyst, sodium nitroprusside (Carl Roth, >99%), and sodium salicylate (Carl Roth, >99%), were prepared. The solutions were prepared fresh weekly and stored at 4 °C in the dark. For the preparation of the salicylate/ catalyst solution, 2 g of sodium salicylate and 8 mg of sodium nitroprusside were dissolved in 15 mL of ultrapure deionized water, to which 5 mL of a 2 M sodium hydroxide solution was added. For the preparation of the hypochlorite solution, 200 µL of sodium hypochlorite solution (12% Cl, Carl Roth) and 1 mL of 2 M NaOH were given to 18.8 mL of water. In a typical testing procedure, 500 µL of the hypochlorite solution were given to 2 mL of the reaction solution, which was filtered through a 0.2 µm syringe filter beforehand. Then, 500 µL of the sodium salicylate solution were added. The mixture was stored in the dark at room temperature overnight for color development, before being analyzed by UV/vis spectroscopy (Perkin Elmer Lambda 750 spectrometer), using a mixture of the two testing solutions and 20% aqueous methanol as reference. For the calibration, ammonium chloride (Carl Roth, >99.7%) stock solutions were prepared in a concentration range from 0.1 µg L^{-1} to 10 mg L^{-1} of NH_4^+. Since the experiment was performed in the presence of methanol as a scavenger, 20% of methanol were present in the calibration as well.

To verify the results from the salicylate test, the filtered reaction solutions were additionally analyzed with *ion chromatography* (IC). A Dionex Aquion System from Thermo Fisher, equipped with a Dionex IonPac CS16 column with a CG16 guard column, CERS suppressor, and electric conductivity detector was employed. 30×10^{-3} M methanesulfonic acid was used as eluent.

Ion chromatography was also used to analyze the reaction solution for nitrate by-products. The reaction solution was filtered with a 0.2 µm syringe filter. A Dionex Aquion system from Thermo Fisher, equipped with a Dionex IonPac AS9-HC column and IonPac AG9-HC guard column was used for the analysis. 1×10^{-3} M $NaHCO_3$/8×10^{-3} M Na_2CO_3 was used as eluent, a UV detector was employed for quantification at a wavelength of 207 nm.

For the quantification of hydrazine, the colorimetric method first reported by Watt and Chrisp was employed.[101] For the testing solution, 0.4 g of *p*-dimethylaminobenzaldehyde (Sigma Aldrich, 99%) were dissolved in 20 mL of ethanol (p.a.), to which 2 mL of concentrated HCl were added. For the calibration curve, standard solutions of hydrazine sulfate (Sigma Aldrich, >99%) in water/methanol mixtures were prepared. For the measurement, 1.5 mL of the filtered reaction solutions were mixed with 1.5 mL of the testing solution and stored in the dark for 20 min for color development, before analysis of the absorbance with UV/vis spectroscopy against a reference containing only the testing solution and a water/methanol mixture.

Supporting Information

Supporting Information is available from the Wiley Online Library or from the author.

Acknowledgements

The authors thank the Bavarian Polymer Institute (BPI), University of Bayreuth, for use of XPS and SEM in the KeyLabs "Device Engineering" and "Electron and Optical Microscopy," respectively. The authors further thank Lena Geiling for TGA-MS measurements, Mirco Ade for SEM and EDX analysis, Silke Hammer for first IC analysis for nitrates, and Anja Hofmann for assistance in the TAS measurements – all University of Bayreuth. J.Z. and R.M. gratefully acknowledge funding in the graduate school of the Bavarian Center for Battery Technology (BayBatt), University of Bayreuth, and by the Bavarian State Ministry of Science, Research and the Arts within the collaborative research network Solar Technologies Go Hybrid.

Open access funding enabled and organized by Projekt DEAL.

Conflict of Interest

The authors declare no conflict of interest.

Data Availability Statement

The data that support the findings of this study are available from the corresponding author upon reasonable request.

Keywords

ammonia, carbon nitride, nitrogen reduction, photocatalysis, pyrite

Received: July 15, 2022
Revised: August 25, 2022
Published online: September 20, 2022

[1] R. Schlögl, *Angew. Chem., Int. Ed.* **2003**, *42*, 2004.
[2] A. J. Medford, M. C. Hatzell, *ACS Catal.* **2017**, *7*, 2624.
[3] J. G. Chen, R. M. Crooks, L. C. Seefeldt, K. L. Bren, R. M. Bullock, M. Y. Darensbourg, P. L. Holland, B. Hoffman, M. J. Janik, A. K. Jones, M. G. Kanatzidis, P. King, K. M. Lancaster, S. V. Lymar, P. Pfromm, W. F. Schneider, R. R. Schrock, *Science* **2018**, *360*, eaar6611.
[4] H. P. Jia, E. A. Quadrelli, *Chem. Soc. Rev.* **2014**, *43*, 547.
[5] A. R. Singh, B. A. Rohr, J. A. Schwalbe, M. Cargnello, K. Chan, T. F. Jaramillo, I. Chorkendorff, J. K. Nørskov, *ACS Catal.* **2017**, *7*, 706.
[6] C. Tang, S. Z. Qiao, *Chem. Soc. Rev.* **2019**, *48*, 3166.
[7] S. Z. Andersen, V. Čolić, S. Yang, J. A. Schwalbe, A. C. Nielander, J. M. McEnaney, K. Enemark-Rasmussen, J. G. Baker, A. R. Singh, B. A. Rohr, M. J. Statt, S. J. Blair, S. Mezzavilla, J. Kibsgaard, P. C. K. Vesborg, M. Cargnello, S. F. Bent, T. F. Jaramillo, I. E. L. Stephens, J. K. Nørskov, I. Chorkendorff, *Nature* **2019**, *570*, 504.
[8] J. Choi, B. H. R. Suryanto, D. Wang, H. L. Du, R. Y. Hodgetts, F. M. Ferrero Vallana, D. R. MacFarlane, A. N. Simonov, *Nat. Commun.* **2020**, *11*, 5546.
[9] D. Ziegenbalg, J. Zander, R. Marschall, *ChemPhotoChem* **2021**, *5*, 792.
[10] X. Wang, K. Maeda, A. Thomas, K. Takanabe, G. Xin, J. M. Carlsson, K. Domen, M. Antonietti, *Nat. Mater.* **2009**, *8*, 76.
[11] W. J. Ong, L. L. Tan, Y. H. Ng, S. T. Yong, S. P. Chai, *Chem. Rev.* **2016**, *116*, 7159.
[12] J. Fu, J. Yu, C. Jiang, B. Cheng, *Adv. Energy Mater.* **2018**, *8*, 1701503.
[13] H. Shi, S. Long, J. Hou, L. Ye, Y. Sun, W. Ni, C. Song, K. Li, G. G. Gurzadyan, X. Guo, *Chem. – Eur. J.* **2019**, *25*, 5028.
[14] H. Katsumata, F. Higashi, Y. Kobayashi, I. Tateishi, M. Furukawa, S. Kaneco, *Sci. Rep.* **2019**, *9*, 14873.
[15] B. Liu, L. Ye, R. Wang, J. Yang, Y. Zhang, R. Guan, L. Tian, X. Chen, *ACS Appl. Mater. Interfaces* **2018**, *10*, 4001.
[16] O. Elbanna, M. Fujitsuka, T. Majima, *ACS Appl. Mater. Interfaces* **2017**, *9*, 34844.
[17] X. Feng, H. Chen, F. Jiang, X. Wang, *J. Colloid Interface Sci.* **2018**, *509*, 298.
[18] A. Kumar, P. Raizada, A. Hosseini-Bandegharaei, V. K. Thakur, V. H. Nguyen, P. Singh, *C-, N-Vacancy Defect Engineered Polymeric Carbon Nitride towards Photocatalysis: Viewpoints and Challenges*, Vol. *9*, Royal Society of Chemistry, London **2021**.
[19] D. Zhao, C. L. Dong, B. Wang, C. Chen, Y. C. Huang, Z. Diao, S. Li, L. Guo, S. Shen, *Adv. Mater.* **2019**, *31*, 1903545.
[20] P. Niu, M. Qiao, Y. Li, L. Huang, T. Zhai, *Nano Energy* **2018**, *44*, 73.

[21] L. Jiang, J. Yang, X. Yuan, J. Guo, J. Liang, W. Tang, Y. Chen, X. Li, H. Wang, W. Chu, *Adv. Colloid Interface Sci.* **2021**, *296*, 102523.
[22] X. Chen, N. Li, Z. Kong, W. J. Ong, X. Zhao, *Mater. Horiz.* **2018**, *5*, 9.
[23] R. Shi, Y. Zhao, G. I. N. Waterhouse, S. Zhang, T. Zhang, *ACS Catal.* **2019**, *9*, 9739.
[24] G. Zhang, Y. Li, C. He, X. Ren, P. Zhang, H. Mi, *Adv. Energy Mater.* **2021**, *11*, 2003294.
[25] X. Li, X. Sun, L. Zhang, S. Sun, W. Wang, *J. Mater. Chem. A* **2018**, *6*, 3005.
[26] H. Ma, Z. Shi, Q. Li, S. Li, *J. Phys. Chem. Solids* **2016**, *99*, 51.
[27] N. Zhou, P. Qiu, H. Chen, F. Jiang, *J. Taiwan Inst. Chem. Eng.* **2018**, *83*, 99.
[28] W. Wang, H. Zhang, S. Zhang, Y. Liu, G. Wang, C. Sun, H. Zhao, *Angew. Chem., Int. Ed.* **2019**, *58*, 16644.
[29] C. Liang, H. Y. Niu, H. Guo, C. G. Niu, D. W. Huang, Y. Y. Yang, H. Y. Liu, B. Bin Shao, H. P. Feng, *Chem. Eng. J.* **2020**, *396*, 125395.
[30] M. Cheng, C. Xiao, Y. Xie, *Photocatalytic Nitrogen Fixation: The Role of Defects in Photocatalysts*, Vol. *7*, Royal Society of Chemistry, London **2019**, 19616.
[31] A. Meng, Z. Teng, Q. Zhang, C. Su, *Chem. – Asian J.* **2020**, *15*, 3405.
[32] V. W. Lau, I. Moudrakovski, T. Botari, S. Weinberger, M. B. Mesch, V. Duppel, J. Senker, V. Blum, B. V. Lotsch, *Nat. Commun.* **2016**, *7*, 12165.
[33] W. B. Tolman, *Activation of Small Molecules: Organometallic and Bioinorganic Perspectives*, Wiley-VCH, **2006**.
[34] J. Liu, M. S. Kelley, W. Wu, A. Banerjee, A. P. Douvalis, J. Wu, Y. Zhang, G. C. Schatz, M. G. Kanatzidis, *Proc. Natl. Acad. Sci. USA* **2016**, *113*, 5530.
[35] K. Chu, Q. Q. Li, Y. H. Cheng, Y. P. Liu, *ACS Appl. Mater. Interfaces* **2020**, *12*, 11789.
[36] C. Chen, Y. Liu, Y. Yao, *Eur. J. Inorg. Chem.* **2020**, *2020*, 3236.
[37] N. F. Lowndes, A. L. Johnson, L. H. Johnston, E. M. Mcintosh, T. Atkinson, R. K. Storms, M. Smith, T. I. Lee, *Science* **2003**, *301*, 76.
[38] J. G. Howalt, T. Vegge, *Phys. Chem. Chem. Phys.* **2013**, *15*, 20957.
[39] J. Wu, Z. X. Wang, S. Li, S. Niu, Y. Zhang, J. Hu, J. Zhao, P. Xu, P. Xu, *Chem. Commun.* **2020**, *56*, 6834.
[40] J. Wang, H. Nan, Y. Tian, K. Chu, *ACS Sustainable Chem. Eng.* **2020**, *8*, 12733.
[41] K. Chu, Y. P. Liu, Y. B. Li, Y. L. Guo, Y. Tian, *ACS Appl. Mater. Interfaces* **2020**, *12*, 7081.
[42] L. Tian, J. Zhao, X. Ren, X. Sun, Q. Wei, D. Wu, *ChemistryOpen* **2021**, *10*, 1041.
[43] S. Shukla, G. Xing, H. Ge, R. R. Prabhakar, S. Mathew, Z. Su, V. Nalla, T. Venkatesan, N. Mathews, T. Sritharan, T. C. Sum, Q. Xiong, *ACS Nano* **2016**, *10*, 4431.
[44] S. Liu, M. Li, S. Li, H. Li, L. Yan, *Appl. Surf. Sci.* **2013**, *268*, 213.
[45] H. Sun, P. Tang, *Adv. Mater. Res.* **2012**, *486*, 55.
[46] M. V. Morales-Gallardo, A. M. Ayala, M. Pal, M. A. Cortes Jacome, J. A. Toledo Antonio, N. R. Mathews, *Chem. Phys. Lett.* **2016**, *660*, 93.
[47] L. Wu, N. Y. Dzade, L. Gao, D. O. Scanlon, Z. Öztürk, N. Hollingsworth, B. M. Weckhuysen, E. J. M. Hensen, N. H. de Leeuw, J. P. Hofmann, *Adv. Mater.* **2016**, *28*, 9602.
[48] H. Qin, J. Jia, L. Lin, H. Ni, M. Wang, L. Meng, *Mater. Sci. Eng. B: Solid-State Mater. Adv. Technol.* **2018**, *236–237*, 104.
[49] S. Kokilavani, A. Syed, L. L. Raju, S. Al-Rashed, A. M. Elgorban, A. M. Thomas, S. S. Khan, *Surf. Interfaces* **2021**, *23*, 101003.
[50] X. Ye, X. Li, X. Chu, Z. Wang, S. Zuo, T. Wang, C. Yao, *J. Alloys Compd.* **2021**, *871*, 159542.
[51] G. Lee, M. Kang, *Curr. Appl. Phys.* **2013**, *13*, 1482.
[52] E. Han, F. Hu, S. Zhang, B. Luan, P. Li, H. Sun, S. Wang, *Energy Fuels* **2018**, *32*, 4357.
[53] T. R. Kuo, H. J. Liao, Y. T. Chen, C. Y. Wei, C. C. Chang, Y. C. Chen, Y. H. Chang, J. C. Lin, Y. C. Lee, C. Y. Wen, S. S. Li, K. H. Lin, D. Y. Wang, *Green Chem.* **2018**, *20*, 1640.
[54] D. Y. Wang, M. Gong, H. L. Chou, C. J. Pan, H. A. Chen, Y. Wu, M. C. Lin, M. Guan, J. Yang, C. W. Chen, Y. L. Wang, B. J. Hwang, C. C. Chen, H. Dai, *J. Am. Chem. Soc.* **2015**, *137*, 1587.
[55] M. Barawi, I. J. Ferrer, E. Flores, S. Yoda, J. R. Ares, C. Sánchez, *J. Phys. Chem. C* **2016**, *120*, 9547.
[56] H. Bin Wang, J. Q. Wang, R. Zhang, C. Q. Cheng, K. W. Qiu, Y. J. Yang, J. Mao, H. Liu, M. Du, C. K. Dong, X. W. Du, *ACS Catal.* **2020**, *10*, 4914.
[57] D. Feng, X. Zhang, Y. Sun, T. Ma, *Nano Mater. Sci.* **2020**, *2*, 132.
[58] C. C. Chang, S. R. Li, H. L. Chou, Y. C. Lee, S. Patil, Y. S. Lin, C. C. Chang, Y. J. Chang, D. Y. Wang, *Small* **2019**, *15*, 1904723.
[59] M. Lashgari, P. Zeinalkhani, *Nano Energy* **2018**, *48*, 361.
[60] B. Wei, C. Wang, Y. He, G. Ran, Q. Song, *Compos. Commun.* **2021**, *24*, 100652.
[61] L. Li, J. Gao, Y. Yuan, S. Zhang, M. Liang, Y. Liu, *J. Taiwan Inst. Chem. Eng.* **2021**, *126*, 134.
[62] F. Fina, S. K. Callear, G. M. Carins, J. T. S. Irvine, *Chem. Mater.* **2015**, *27*, 2612.
[63] B. V. Lotsch, M. Döblinger, J. Sehnert, L. Seyfarth, J. Senker, O. Oeckler, W. Schnick, *Chem. – Eur. J.* **2007**, *13*, 4969.
[64] E. Alwin, W. Nowicki, R. Wojcieszak, M. Zieliński, M. Pietrowski, *Dalt. Trans.* **2020**, *49*, 12805.
[65] T. Sano, S. Tsutsui, K. Koike, T. Hirakawa, Y. Teramoto, N. Negishi, K. Takeuchi, *J. Mater. Chem. A* **2013**, *1*, 6489.
[66] B. Choudhury, K. K. Paul, D. Sanyal, A. Hazarika, P. K. Giri, *J. Phys. Chem. C* **2018**, *122*, 9209.
[67] G. Dong, W. Ho, C. Wang, *J. Mater. Chem. A* **2015**, *3*, 23435.
[68] S. Wang, J. Zhan, K. Chen, A. Ali, L. Zeng, H. Zhao, W. Hu, L. Zhu, X. Xu, *ACS Sustainable Chem. Eng.* **2020**, *8*, 8214.
[69] H. Wang, M. Li, H. Li, Q. Lu, Y. Zhang, S. Yao, *Mater. Des.* **2019**, *162*, 210.
[70] H. Li, Z. Zhang, Y. Liu, W. Cen, X. Luo, *Nanomaterials* **2018**, *8*, 4.
[71] G. Zhang, G. Li, Z. A. Lan, L. Lin, A. Savateev, T. Heil, S. Zafeiratos, X. Wang, M. Antonietti, *Angew. Chem, Int. Ed.* **2017**, *56*, 13445.
[72] Z. Sun, S. Wang, Q. Li, M. Lyu, T. Butburee, B. Luo, H. Wang, J. M. T. A. Fischer, C. Zhang, Z. Wu, L. Wang, *Adv. Sustain. Syst.* **2017**, *1*, 1700003.
[73] H. Yu, R. Shi, Y. Zhao, T. Bian, Y. Zhao, C. Zhou, G. I. N. Waterhouse, L.-Z. Wu, C.-H. Tung, T. Zhang, *Adv. Mater.* **2017**, *29*, 1605148.
[74] M. Kim, S. Hwang, J. S. Yu, *J. Mater. Chem.* **2007**, *17*, 1656.
[75] K. Akaike, K. Aoyama, S. Dekubo, A. Onishi, K. Kanai, *Chem. Mater.* **2018**, *30*, 2341.
[76] C. Lv, Y. Qian, C. Yan, Y. Ding, Y. Liu, G. Chen, G. Yu, *Angew. Chem., Int. Ed.* **2018**, *57*, 10246.
[77] Y. Zhao, R. Shi, X. Bian, C. Zhou, Y. Zhao, S. Zhang, F. Wu, G. I. N. Waterhouse, L. Wu, C. Tung, T. Zhang, *Adv. Sci.* **2019**, *6*, 1802109.
[78] N. Suzuki, R. Kuroda, *Analyst* **1987**, *112*, 1077.
[79] Y. Ozaki, S. Kawata, *Far- and Deep-Ultraviolet Spectroscopy*, Springer, Japan **2015**.
[80] Y. Mu, Y. Peng, R. A. Lauten, *Miner. Eng.* **2016**, *96–97*, 143.
[81] R. Godin, Y. Wang, M. A. Zwijnenburg, J. Tang, J. R. Durrant, *J. Am. Chem. Soc.* **2017**, *139*, 5216.
[82] K. L. Corp, C. W. Schlenker, *J. Am. Chem. Soc.* **2017**, *139*, 7904.
[83] Y. Wang, X. Liu, X. Han, R. Godin, J. Chen, W. Zhou, C. Jiang, J. F. Thompson, K. B. Mustafa, S. A. Shevlin, J. R. Durrant, Z. Guo, J. Tang, *Nat. Commun.* **2020**, *11*, 2531.
[84] G. Peng, J. Albero, H. Garcia, M. Shalom, *Angew. Chem, Int. Ed.* **2018**, *57*, 15807.
[85] H. Kisch, *Angew. Chem, Int. Ed.* **2013**, *52*, 812.
[86] C. Merschjann, S. Tschierlei, T. Tyborski, K. Kailasam, S. Orthmann, D. Hollmann, T. Schedel-Niedrig, A. Thomas, S. Lochbrunner, *Adv. Mater.* **2015**, *27*, 7993.

[87] W. Wang, X. Bai, Q. Ci, L. Du, X. Ren, D. L. Phillips, *Adv. Funct. Mater.* **2021**, *31*, 2103978.
[88] Y. Jiao, R. Hu, Q. Wang, F. Fu, L. Chen, Y. Dong, Z. Lin, *Chem. – Eur. J.* **2021**, *27*, 10925.
[89] P. Wu, J. Wang, J. Zhao, L. Guo, F. E. Osterloh, *J. Mater. Chem. A* **2014**, *2*, 20338.
[90] H. Zhang, A. Yu, *J. Phys. Chem. C* **2014**, *118*, 11628.
[91] A. B. Jorge, D. J. Martin, M. T. S. Dhanoa, A. S. Rahman, N. Makwana, J. Tang, A. Sella, F. Corà, S. Firth, J. A. Darr, P. F. McMillan, *J. Phys. Chem. C* **2013**, *117*, 7178.
[92] Z. Gan, Y. Shan, J. Chen, Q. Gui, Q. Zhang, S. Nie, X. Wu, *Nano Res.* **2016**, *9*, 1801.
[93] R. M. Jay, J. Norell, S. Eckert, M. Hantschmann, M. Beye, B. Kennedy, W. Quevedo, W. F. Schlotter, G. L. Dakovski, M. P. Minitti, M. C. Hoffmann, A. Mitra, S. P. Moeller, D. Nordlund, W. Zhang, H. W. Liang, K. Kunnus, K. Kubiček, S. A. Techert, M. Lundberg, P. Wernet, K. Gaffney, M. Odelius, A. Föhlisch, *J. Phys. Chem. Lett.* **2018**, *9*, 3538.
[94] M. Kostovic, D. Vucinic, *Physicochem. Probl. Miner. Process.* **2016**, *52*, 609.
[95] S. C. Yan, Z. S. Li, Z. G. Zou, *Langmuir* **2009**, *25*, 10397.
[96] P. Kubelka, F. Munk, *Z. Tech. Phys* **1931**, *265*, 593.
[97] J. Tauc, *Mater. Res. Bull.* **1968**, *3*, 37.
[98] F. Zhou, L. M. Azofra, M. Ali, M. Kar, A. N. Simonov, C. McDonnell-Worth, C. Sun, X. Zhang, D. R. Macfarlane, *Energy Environ. Sci.* **2017**, *10*, 2516.
[99] C. E. Bower, T. Holm-Hansen, *Can. J. Fish. Aquat. Sci.* **1980**, *37*, 794.
[100] M. Krorn, *Analyst* **1980**, *105*, 305.
[101] G. W. Watt, J. D. Chrisp, *Anal. Chem.* **1952**, *24*, 2006.